Quantitative PET/CT imaging and dosimetry of 89Zr labelled compounds

Makris, N.

2015

document version
Publisher's PDF, also known as Version of record

1

Introduction

In 1928, Paul Dirac proposed that electrons could have either a positive or a negative charge (1), although without explicitly predicting a new particle. Four years later, Carl D. Anderson recorded one of the first cosmic ray photographs of a positively charged electron (2) that led to the discovery of the positron and corroborated Dirac's theory. After another two decades, Wrenn et al. (3) were the first to describe coincidence counting and its application to positron scanning. This electronic collimation was implemented by Anger (4), who is known primarily for the first single photon gamma camera, but who later shifted his focus onto positron imaging, developing a dual detector positron emission tomography (PET) scanner. However, it was used for only a brief period, as the first clinical data pointed to the problem of undersampling. Although omission of lead or tungsten collimators increased the number of detected photons by at least an order of magnitude compared with single photon imaging, the fraction of coincident events was only 1%, indicating the need for a higher singles count rate capability. Other attempts include those of Brownell and his group, who developed a series of instruments over several decades. These instruments ranged from dual planar detectors (5), operating in coincidence mode and providing longitudinal tomographic images, to rotating detectors that used transverse reconstruction techniques and, finally, to complete circular stationary detector arrangements, first with a single slice (6) and subsequently with a large number of transverse slices (7). Ter-Pogossian et al. (8) and Phelps et al. (9) were among the first to build a transaxial PET scanner at the Washington University; Subsequently, several improvements were introduced (10,11) followed by the first commercial PET scanner, the ECAT, by Phelps et al. (12). At that time, all systems had a one to one coupling with large NaI crystals and their size primarily determined spatial resolution. A major breakthrough towards improved spatial resolution was the introduction of the block detector by Casey and Nutt (13), where the block consisted of many smaller crystals and where Anger logic was used for crystal identification. A couple of years later, iterative reconstruction algorithms became more generally used, leading to improved image quality of both emission and transmission scans. More recently, in 2000, a hybrid modality, combining PET and computed tomography (CT), was introduced (14) and it has already shown its value in several clinical areas such as oncology (15, 16) and cardiology (17,18). The merger of PET and magnetic resonance (MR) is also feasible, either in a way that the images are serially obtained or in a true integrated manner that allows for simultaneous acquisition of PET and MR data. The latter combination was realized after the development of MR compatible PET detectors (19, 20). Although MR based PET attenuation

correction techniques still require improvements to guarantee quantitatively accurate PET data, and more studies are still needed to establish and validate PET/MRs clinical role, yet, it shows a clear benefit over PET/CT in applications that demand high soft tissue contrast, low radiation dose and multiparametric imaging (21)

1.1 Positron emission tomography

Positron emission tomography is a non-invasive diagnostic modality that makes use of biological compounds labelled with a positron emitting radionuclide, such as short-lived ^{18}F, ^{15}O, and ^{11}C, or long-lived ^{89}Zr, ^{124}I and ^{86}Y. A scan procedure starts with the injection of a tracer amount of the radiolabelled compound into the patient, which over time distributes throughout the body. This distribution can be measured in selected time frame(s) and information on glucose consumption, blood flow, tumour cell proliferation, or receptor expression can be derived, depending on the radiolabelled compound used. The radioactive nucleus decays over time by converting a proton into a neutron, which results in the emission of a positron. Subsequently, the positron travels through the tissue until its kinetic energy decreases to a point where it combines with an electron. This complex of electron and positron is very unstable, resulting in the almost instantaneous annihilation of both particles, dissipating their energy in the form of two 511 keV photons that are emitted in essentially opposite directions. Simultaneous (coincidence) detection of the two photons by scintillation crystals coupled to photomultiplier tubes assigns the annihilation event to a line-of-response (LOR) joining the two in coincidence detectors. The latest generation detectors, with timing resolution of 500-800 ns, is able to more accurately localize the annihilation event along a LOR (within a few cm), thereby essentially improving signal-to-noise ratios leading to increased lesion detectability (22, 23). By the end of a scan, a vast number (~10^9) of LORs are collected and then sorted out into sinograms, which are used as input for image reconstruction. All the coincidence events are collectively called prompts which include true, random, and scattered events. A true coincidence event occurs when two 511 keV photons from a single annihilation event are detected by a detector pair along the LOR (Figure 1.1a). Scatter coincidences may be caused by Compton scattering of one or both annihilation photons in the body (Figure 1.1b), resulting in the identification of an erroneous LOR.

In order to correct for such false coincidences, a scatter simulation algo-

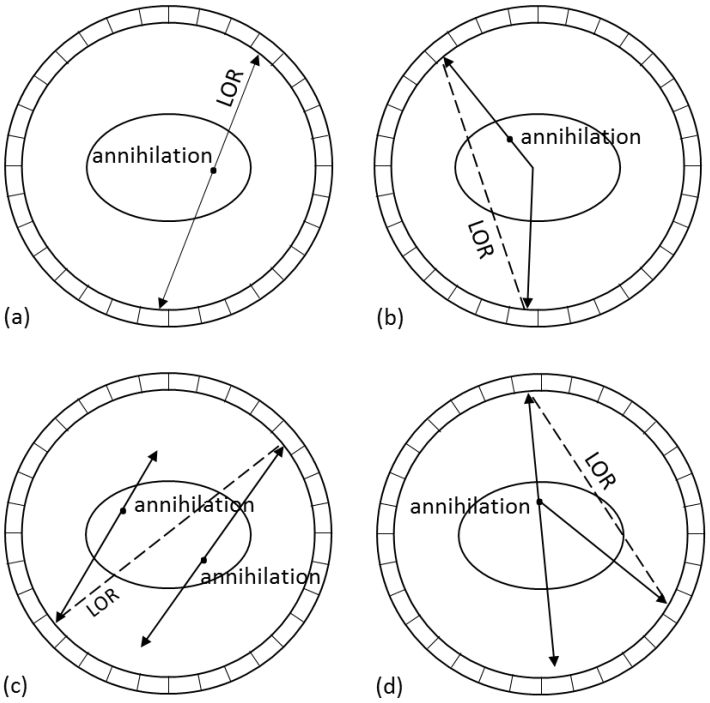

Figure 1.1.
Schematic representation of different coincidences: (a) true, (b) scattered, (c) random coincidences and (d) annihilation photon-cascade γ photon coincidence. LOR: line-of-response.

rithm is used to estimate the scatter contribution (24). Another contribution to false coincidences is the simultaneous detection of two photons originating from different annihilation events, called random coincidences (Figure 1.1c). There are two ways to remove random events: a) by calculating the random event rate from singles measurements and b) by applying a delayed coincidence timing window. Especially at high count rates, the contribution of random coincidences can be significant, as they increase quadratically with tracer activity, whereas true coincidences increase linearly. Finally, there is a probability that one of the annihilation photons is absorbed in the body. The probability of attenuation does not depend on the source position but on the total path length of the two annihilation photons in the body. Thus, for each line of response, correction factors can be derived from a transmission scan, measuring its attenuation using, for example, an external rotating radiation source. To date, most scanners are hybrid PET/CT scanners and the CT data can be used to correct the corresponding PET data for attenuation. CT based attenuation correction offers certain advantages over transmission based attenuation correction, as it combines statistical quality and spatial resolution of CT data with short scanning times. Corrections

for scatter and random coincidences as well as for attenuation in the human body allow for the reconstruction of quantitatively accurate PET images, which subsequently can be used to quantify tissue functions.

1.2 Standardization and harmonization of (multicentre) PET studies

Absolute radiotracer quantification in oncological PET studies can only be achieved through the use of a dynamic scan. Subsequent reconstruction into several time frames provides the radiotracer distribution at the corresponding time points. However, this procedure is labor and time consuming, and requires a significant amount of time for data analysis to derive fully quantitative outcome measures. Therefore, often a simple semi-quantitative measure, the standardized uptake value (SUV), is used in many routine PET/CT examinations. The main advantages of SUV for clinical studies are that it only requires a static (single) scan and no arterial blood sampling. SUV is equal to the radioactivity concentration in the tissue of interest normalized to injected dose and patient weight. SUV measures are used widely in ^{18}F-fluorodeoxyglucose ([^{18}F]FDG) PET/CT studies, as they allow for a simple assessment of a patient's response to therapy. These measurements may play an important role as prognostic factors in patients with lung and gastrointestinal cancer (25). However, several factors may introduce bias in obtained SUV measurements (26, 27). The increasing number of PET/CT systems has allowed for the conduction of multicentre trials (e.g. ARTFORCE (28) and IMPACT trials), accelerating recruitment of patients, which is of particular importance in the case of rare diseases. Although pooling of PET data should enable larger patient trials within a shorter period of time, non-standardized data acquisition and image analysis procedures across centres may lead to incomparable SUVs (29). It is well known that different PET/CT scanners with corresponding image analysis platforms cannot always use common parameters due to differences in (implementation of) algorithms. To overcome these problems, harmonized acquisition and data analysis procedures can be used to provide comparable and interchangeable SUV measures between institutes. To this end acquisition, reconstruction and analysis settings are defined for each centre in order to produce harmonized image characteristics and SUVs. This can be achieved by implementing a cross-calibration procedure across institutes participating in a clinical trial (30, 31). Nevertheless, residual differences in SUVs between institutes may still be present, even after a rigorous quality

control procedure. To further reduce SUV differences between centers, data analysis procedures should be used that are insensitive to changes in (quantitative) image characteristics (32). Even though harmonization is essential for a meaningful comparison of SUV measures within a clinical trial, it may also limit the advantages that new technologies provide such as new reconstruction algorithms, time-of-flight (TF) capability, etc. In addition, it may reduce PET/CT image quality, which is a significant drawback for visual inspection. To tackle this problem, a simple procedure has been proposed by Lasnon et al. (33) in which two image data sets are generated for each clinical scan, one is based on parameters derived from the harmonization procedure, meeting the EANM FDG PET/CT guidelines for multicentre trials (31), the other exploiting all (novel) local features (TF, point spread function reconstruction) available at a certain centre to generate the best possible images for visual inspection (33).

1.3 ImmunoPET

New insights into our understanding of cancer cell biology has provided the opportunity to identify new molecular targets on tumour cells, such as those involved in apoptosis, proliferation, angiogenesis and differentiation. Based on these new molecular targets, research on the development of targeted pharmaceuticals and more specifically on the synthesis of new monoclonal antibodies (mAb) has been ongoing, resulting in several mAbs used in molecular imaging and targeted therapy (34), such as:

• Cetuximab (Erbitux^{TM}) directed against epidermal growth factor receptor (EGFR) and used in treatment of colorectal cancer and head and neck cancer.

• Rituximab (Rituxan^{TM}) and ^{90}Y-Ibritumomab tiuxetan (Zevalin^{TM}) targeting CD20 and approved in Non-Hodgkin's lymphoma therapy.

• Trastuzumab (Herceptin^{TM}) targeting human epidermal growth factor receptor 2 (HER2) and approved for treatment of breast cancer and gastric cancer.

• Bevacizumab (Avastin^{TM}) directed against vascular endothelial growth factor (VEGF) and used in colorectal cancer, non-small cell lung cancer, breast, and ovarian cancer treatment.

Although the advent of new targeted pharmaceuticals has paved the way for new treatments of cancer, it also poses challenges on how to test and improve efficacy of targeted drugs, such as how to identify those patients who would benefit from treatment with these drugs, and how to improve the

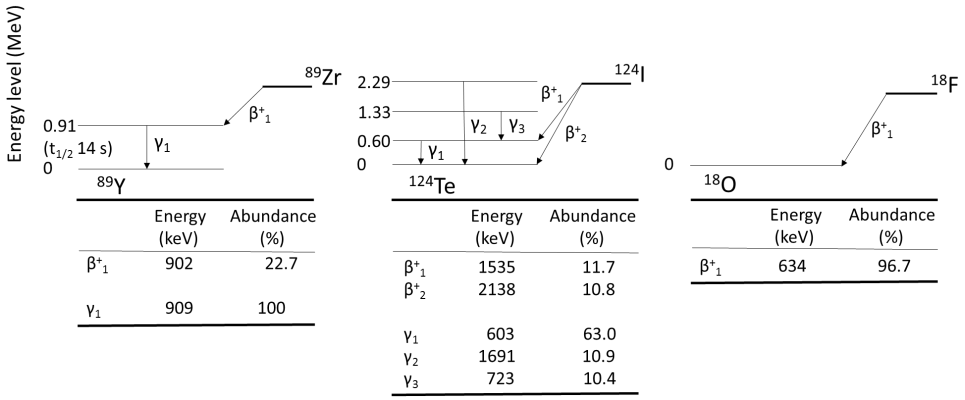

	Energy (keV)	Abundance (%)
β^+_1	902	22.7
γ_1	909	100

	Energy (keV)	Abundance (%)
β^+_1	1535	11.7
β^+_2	2138	10.8
γ_1	603	63.0
γ_2	1691	10.9
γ_3	723	10.4

	Energy (keV)	Abundance (%)
β^+_1	634	96.7

Figure 1.2. *Simplified decay schemes for ^{18}F, ^{89}Zr and ^{124}I. Only radiation with an abundance > 5%*

efficacy of drug development in order to minimize the costs of such drugs. *In vivo* information on the behavior of those drugs is of utmost importance, as it can give further insight in the targeting of tumours and uptake in critical organs to assess radiotoxicity. This can be achieved by labelling these targeted drugs with positron emitting radionuclides, and measuring their uptake using PET, so-called immunoPET. The physical characteristics of the selected radionuclides should match the kinetic behavior of the drug. In other words, intact mAbs are characterized by slow kinetics, typically several days, dictating the use of long-lived positron emitters to optimally visualize them using PET. The most commonly used long-lived positron emitters are ^{89}Zr ($t_{1/2}$ = 78.4 h) and ^{124}I ($t_{1/2}$ = 100.3 h) (Figure 1.2). The potential of immunoPET has not yet been explored adequately in clinical practice. Nevertheless, a series of prospective studies (35–40) has already shown its potential in drug development and its ability in predicting biodistribution and tumour targeting prior to immunotherapy (41).

1.4 Quantitative PET/CT with long-lived radionuclides

^{18}F has an ideal decay scheme, emitting positrons with an abundance of nearly 100% and with no simultaneous γ emissions. In contrast, ^{89}Zr and especially ^{124}I show a complex decay scheme along with a low positron abundance (~23%). As seen in Figure 1.2, in the case of ^{124}I, ~50% of the positrons are associated with simultaneous emission of 603 keV cascade γ photons, and the latter may hamper quantification and image quality. More specifically, the detection of false coincidences represented by either a

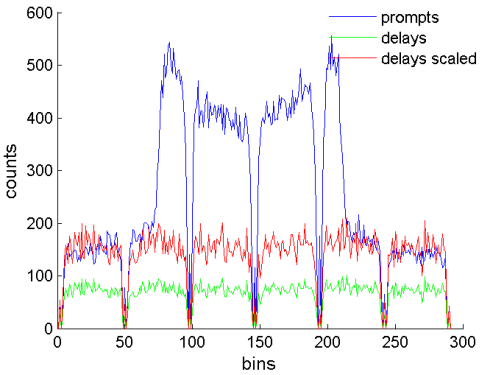

Figure 1.3. *Verification of the randoms estimation in ^{124}I PET by comparing the background of prompt and delayed sinograms. The green profile does not match with the blue profile and shows that the delay sinogram may be underestimated. This is due to the cascade gamma coincidence. A scaling factor can be calculated by matching the counts of prompt and delay outside of the object (phantom). The red profile shows that the delays are scaled to match the expected random.*

cascade γ photon and an annihilation photon Figure 1.1d or two cascade γ photons will introduce bias in a PET image. Previously, it has been reported that a spatially uniform profile provides a sufficient description of the cascade γ photon coincidences (42, 43), and thus a simple and straightforward way to correct for such coincidences would be by scaling the delays profile in order to match the counts of the prompts profile outside of the object (Figure 1.3). However, a simulation study (44) has shown that the assumption of a spatially uniform profile may be a crude estimate and, therefore, a dedicated cascade γ photon correction combined (to account for false coincidences) following the single scatter simulation algorithm should be used to provide more reliable results. Other correction methods for this effect include a convolution subtraction algorithm (45) and a point-spread function subtraction (46). In the case of ^{124}I, rejection of photons outside the energy window of the PET scanner does contribute to the dead time of the system. However, since these photons do not contribute to the recorded singles count rate, the dead time correction may be inaccurate (47). In the case of ^{89}Zr, fewer challenges will be posed in quantification and image quality. Given the non simultaneous emission of 909 keV γ photons and positrons, an increased randoms coincidence rate can be expected, leading to increased image noise, but not to quantitative bias. However, care should be taken with respect to the cross calibration between dose calibrator and PET scanner.

1.5 VOI definition methods

Acquisition and reconstruction of PET data is followed by the derivation of quantitative measures, starting with the delineation of organ volumes and/or tumours volumes, i.e. volumes of interest (VOI). Various VOI definition methods can be used, using manually defined VOI boundaries or

semiautomated 3D region growing techniques that are based on a fixed or relative threshold ($SUV_{A50\%}$), maximum uptake (SUV_{max}), and fixed size region (SUV_{3Dpeak}). Yet, SUV variability, especially for very small (tumour) volumes, may be present in those simple VOI definition techniques, and more sophisticated VOI segmentation techniques (i.e. gradient based) that are fully automated and observer independent have been developed to match with pathological findings. Although those VOI segmentation techniques may have certain advantages, their implementation is not straightforward and their limited use throughout PET centres will compromise any possibility for harmonized SUV quantification.

1.6 Internal radiation dosimetry

Absorbed fraction dosimetry can be used to calculate the radiation dose delivered to a target organ from radioactivity contained in one or more source organs in the body. To estimate absorbed doses for all critical tissues, the energy absorbed per unit mass for each tissue should be determined. Another important parameter is the fraction of emitted energy (ϕ) that is absorbed by the target region. Depending on the type radiation emitted, ϕ will be assigned a value between 0 and 1. For electrons and beta particles (non-penetrating radiation), the energy will be absorbed by the target region, and, therefore, ϕ is set equal to 1. In contrast, for photons (penetrating radiation), part of the emitted energy will escape and be absorbed by regions adjacent to the target tissue. For photons, the absorbed fraction increases with the cube root of the mass for self irradiation (source organ = target organ) if the photon mean pathlength is large compared with the organ diameter whereas for cross-irradiation (source organ ≠ target organ) the photon absorbed fractions vary directly with the mass (48). The absorbed dose in any target organ is given by the following equation:

$$\dot{D} = \frac{k\tilde{A}\sum_{i} n_i E_i \phi_i}{m} \tag{1.1}$$

where D is the absorbed dose in a target organ (Gy), $\tilde{A}$ the cumulated activity in a source organ, n the number of radiations with energy E emitted per nuclear transition, E the energy per radiation (MeV), i the number of radiations in the decay scheme of a radionuclide, ϕ the fraction of energy emitted that is absorbed in the target region, m the mass of the target region (kg) and k the proportionality constant ($Gy{\cdot}kg{\cdot}MBq^{-1}{\cdot}sec^{-1}{\cdot}MeV^{-1}$).

In most applications of radio-immunotherapy, bone marrow can be the dose limiting organ. Traditionally, blood or plasma activity concentrations at multiple time points after administration are used to estimate absorbed dose in bone marrow (49). This assumes that the intravenously injected activity is distributed uniformly throughout the plasma and the extracellular fluid space of red marrow. Therefore, the activity concentration ratio of red marrow to plasma should be constant and equal to the fraction of red marrow composed of extracellular fluid. The latter approach is used for agents that do not specifically bind to bone marrow cellular components. However, Hindorf et al. (50) have shown that a non-constant red marrow to plasma activity concentration ratio may better describe the kinetics of ^{131}I labelled anti-CD22 mAb while using scintigraphic imaging. Similar findings were reported by Schwartz et al. (51) for ^{124}I-cG250 and ^{124}I-huA33. In the latter study, it was shown that the plasma based approach for estimating bone marrow absorbed dose may introduce discrepancies of as much as –74% to +62% in individual patients for self red marrow dose, as compared to PET image based dosimetry where red marrow activity concentrations were obtained from consecutive static PET scans. Therefore, a PET image based approach or one combined with plasma data (51) may be used to account for a non-constant red marrow to plasma activity concentration ratio, exploiting at the same time the advantage of a robust CT-based VOI delineation. An alternative CT image based approach using an active contour model (52) has been proposed to delineate selectively (part of) the bone marrow, as it is automatic and relatively faster compared to manual VOI delineation.

1.7 Thesis outline

Chapter 2 describes evaluation strategies for harmonizing ^{18}F-FDG PET/CT studies in a multicentre setting and investigates their ability to produce harmonized recovery coefficients and SUV measures. The theme of **Chapter 3** is the same, but here feasibility of quantitative accuracy and harmonized image quality is investigated for multicentre ^{89}Zr PET/CT studies. **Chapter 4** describes the assessment of biodistribution and radiation dosimetry of ^{89}Zr-cetuximab in humans, together with a comparison of image and plasma based red marrow dose estimation approaches. **Chapter 5** describes the development and validation of simplified organ delineation methods in ^{89}Zr labelled mAb PET/CT studies that would guarantee accurate localization of delineated organ VOIs and subsequent accurate estimation of organ absorbed doses. In **Chapter 6** manual and automatic delineation methods are

compared with respect to accurate delineation of bone marrow in the lumbar vertebrae. In addition, associated impact on estimating bone marrow activity concentration and absorbed dose is investigated.

References

[1] P.A.M. Dirac. The quantum theory of the electron. *Proceedings of the Royal Society of London*, 117:610–624, 1928.

[2] C.D. Anderson. The positive electron. *Physical Review*, 43:491–494, 1933.

[3] F.R. Wrenn, M.L. Good, and P. Handler. The use of positron-emitting radioisotopes for the localization of brain tumors. *Science*, 113:525–527, 1951.

[4] H. Anger. Survey of radioisotope cameras. *J Nucl Med*, 5:311–314, 1966.

[5] G.L. Brownell, C.A. Burnham, S. Wilensky, S. Arnonow, H. Kaemi, and D. Strieder. New developements in positron scintigraphy and the application of cyclotron-produced positron emitter. *Medical Radioisotope Scintigraphy(IAEA Proceedings of a Symposium (Salzburg, Austria, August 1968))*, pages 163–176, 1969.

[6] C. Burnham, J. Bradsham, D. Kaufman, D. Chesler, and G.L. Brownell. A positron tomograph employing a one dimension bgo scintillation camera. *IEEE Trans Nucl Science*, 30:661–664, 1983.

[7] C.A. Burnham, J. Bradsham, D. Kaufman, D.A. Chesler, C.W. Stearns, and G.L. Brownell. Design of a cylindrical shaped scintillation camera for positron tomographs. *IEEE Trans Nucl Science*, 32:889–893, 1985.

[8] M.M. Ter-Pogossian, M.E. Phelps, E.J. Hoffman, and N.A. Mullani. A positron-emission transaxial tomograph for nuclear imaging (pett). *Radiology*, 114:89–98, 1975.

[9] M.E. Phelps, E.J. Hoffman, N.A. Mullani, and M.M Ter-Pogossian. Application of annihilation coincidence detection to transaxial reconstruction tomography. *J Nucl Med*, 16:210–224, 1975.

[10] M.E. Phelps, E.J. Hoffman, N.A. Mullani, C.S. Higgins, and M.M. Ter-Pogossian. Design considerations for a positron emission transaxial tomography (pett iii). *IEEE Trans Nucl Science*, 23:516–522, 1976.

[11] M.M. Ter-Pogossian, N.A. Mullani, J.T. Hood, C.S. Higgins, and D.C. Ficke. Design considerations for a positron emission transverse tomograph (pett v) for imaging of the brain. *IEEE Trans Nucl Science*, 2:539–544, 1978.

[12] M.E. Phelps, E.J. Hoffman, S.C. Huang, and D.E. Kuhl. Ecat: a new computerized tomographic imaging system for positron emitting radiopharmaceuticals. *J Nucl Med*, 19:635–647, 1978.

[13] M.E. Casey and R. Nutt. A multicrystal two dimensional bgo detector system for positron emission tomography. *IEEE Trans Nucl Science*, 2:460–463, 1986.

[14] T. Beyer, D.W. Townsend, and T. Brun. A combined pet/ct scanner for clinical oncology. *J Nucl Med*, 41:1369–1379, 2000.

[15] G. Antoch, J. Stattaus, A.T. Nemat, S. Marnitz, T. Beyer, H. Kuehl, A. Bockisch, J.F. Debatin, and L.S. Freudenberg. Non-small cell lung cancer: dual-modality pet/ct in preoperative staging. *Radiology*, 229:526–533, 2003.

[16] R. Bar-Shalom, N. Yefremov, L. Guralnik, D. Gaitini, A. Frenkel, A. Kuten, H. Altman, Z. Keidar, and O. Israel. Clinical performance of pet/ct in evaluation of cancer: additional value for diagnostic imaging and patient management. *J Nucl Med*, 44: 1200–1209, 2003.

[17] M.F. Di Carli, S. Dorbala, J. Meserve, F.G. El, A. Sitek, and S.C. Moore. Clinical myocardial perfusion pet/ct. *J Nucl Med*, 48:783–793, 2007.

[18] M. Namdar, T.F. Hany, P. Koepfli, P.T. Siegrist, C. Burger, C.A. Wyss, T.F. Luscher, G.K. von Schulthess, and P.A. Kaufmann. Integrated pet/ct for the assessment of coronary artery disease: a feasibility study. *J Nucl Med*, 46:930–935, 2005.

[19] B.J. Pichler, M.S. Judenhofer, C. Catana, J.H. Walton, M. Kneilling, R.E. Nutt, S.B. Siegel, C.D. Claussen, and S.R. Cherry. Performance test of an lso-apd detector in a 7-t mri scanner for simultaneous pet/mri. *J Nucl Med*, 47:639–647, 2006.

[20] D.R. Schaart, H.T. van Dam, S. Seifert, R. Vinke, P. Dendooven, H. Lhner, and F.J. Beekman. A novel, sipm-array-based, monolithic scintillator detector for pet. *Phys Med Biol*, 54:3501–3512, 2009.

[21] B.J. Pichler, A. Kolb, T. Nagele, and H.P. Schlemmer. Pet/mri: paving the way for the next generation of clinical multimodality imaging applications. *J Nucl Med*, 51: 333–336, 2010.

[22] S. Surti, J.S. Karp, L.M. Popescu, M.E. Daube-Witherspoon, and M. Werner. Investigation of time-of-flight benefit for fully 3-d pet. *IEEE Trans Med Imaging*, 25: 529–538, 2006.

[23] J.S. Karp, S. Surti, M.E. Daube-Witherspoon, and G. Muehllehner. Benefit of time-of-flight in pet: experimental and clinical results. *J Nucl Med*, 49:462–470, 2008.

[24] C.C. Watson. New, faster, image-based scatter correction for 3d pet. *IEEE Trans Nucl Science*, 47:1587–1594, 2000.

[25] T. Gupta, Z. Master, S. Kannan, J.P. Agarwal, S. Ghsoh-Laskar, V. Rangarajan, V. Murthy, and A. Budrukkar. Diagnostic performance of post-treatment fdg pet or fdg pet/ct imaging in head and neck cancer: a systematic review and meta-analysis. *Eur J Nucl Med Mol Imaging*, 38:2083–2095, 2011.

[26] R. Boellaard, N.C. Krak, O.S. Hoekstra, and A.A. Lammertsma. Effects of noise, image resolution, and roi definition on the accuracy of standard uptake values: a simulation study. *J Nucl Med*, 45:1519–1527, 2004.

[27] N.C. Krak, R. Boellaard, O.S. Hoekstra, J.W. Twisk, C.J. Hoekstra, and A.A. Lammertsma. Effects of roi definition and reconstruction method on quantitative outcome and applicability in a response monitoring trial. *Eur J Nucl Med Mol Imaging*, 32: 294–301, 2005.

[28] J. Heukelom, O. Hamming, H. Bartelink, F. Hoebers, J. Giralt, T. Herlestam, M. Verheij, M. van den Brekel, W. Vogel, N. Slevin, E. Deutsch, J.J. Sonke, P. Lambin, and C. Rasch. Adaptive and innovative radiation treatment for improving cancer treatment outcome (artforce); a randomized controlled phase ii trial for individualized treatment of head and neck cancer. *BMC Cancer*, 13:84, 2013.

[29] J.A. Thie. Understanding the standardized uptake value, its methods, and implications for usage. *J Nucl Med*, 45:1431–1434, 2004.

[30] R. Boellaard. Standards for pet image acquisition and quantitative data analysis. *J Nucl Med*, 50:11S–20S, 2009.

[31] R. Boellaard, M.J. O'Doherty, W.A. Weber, F.M. Mottaghy, M.N. Lonsdale, S.G. Stroobants, W.J. Oyen, J. Kotzerke, O.S. Hoekstra, J. Pruim, P.K. Marsden, K. Tatsch, C.J. Hoekstra, E.P. Visser, B. Arends, F.J. Verzijlbergen, J.M. Zijlstra, E.F. Comans, A.A. Lammertsma, A.M. Paans, A.T. Willemsen, T. Beyer, A. Bockisch, C. Schaefer-Prokop, D. Delbeke, R.P. Baum, A. Chiti, and B.J. Krause. Fdg pet and pet/ct: Eanm procedure guidelines for tumour pet imaging: version 1.0. *Eur J Nucl Med Mol Imaging*, 37:181–200, 2010.

[32] M.D. Kelly and J.M. Declerck. Suvref: reducing reconstruction-dependent variation in pet suv. *EJNMMI Res*, 1:16, 2011.

[33] C. Lasnon, C. Desmonts, E. Quak, R. Gervais, P. Do, C. Dubos-Arvis, and N. Aide. Harmonizing suvs in multicentre trials when using different generation pet systems: prospective validation in non-small cell lung cancer patients. *Eur J Nucl Med Mol Imaging*, 40:985–996, 2013.

[34] L.H. Mammatas, H.M. Verheul, N.H. Hendrikse, M. Yaqub, A.A. Lammertsma, and C.W. Menke van der Houven van Oordt. Molecular imaging of targeted therapies with positron emission tomography: the visualization of personalized cancer care. *Cell Oncol*, DOI:10.1007/s13402-014-0194-4, 2014.

[35] P.K. Borjesson, Y.W. Jauw, R. de Bree, J.C. Roos, J.A. Castelijns, C.R. Leemans, G.A. van Dongen, and R. Boellaard. Radiation dosimetry of 89zr-labeled chimeric monoclonal antibody u36 as used for immuno-pet in head and neck cancer patients. *J Nucl Med*, 50:1828–1836, 2009.

[36] J.A. Carrasquillo, N. Pandit-Taskar, J.A. O'Donoghue, J.L. Humm, P. Zanzonico, P.M. Smith-Jones, C.R. Divgi, D.A. Pryma, S. Ruan, N.E. Kemeny, Y. Fong, D. Wong, T.S. Jaggi, D.A. Scheinberg, M. Gonen, K.S. Panageas, G. Ritter, A.A. Jungbluth, L.J. Old, and S.M. Larson. (124)i-hua33 antibody pet of colorectal cancer. *J Nucl Med*, 52:1173–1180, 2011.

[37] E.C. Dijkers, T.H. Oude Munnink, J.G. Kosterink, A.H. Brouwers, P.L. Jager, J.R. de Jong, G.A. van Dongen C.P. Schrder, M.N. Lub de Hooge, and E.G. de Vries. Biodistribution of 89zr-trastuzumab and pet imaging of her2-positive lesions in patients with metastatic breast cancer. *Clin Pharmacol Ther*, 87:586–592, 2010.

[38] L.R. Perk, O.J. Visser, W.M. Stigter-van, M.J. Vosjan, G.W. Visser, J.M. Zijlstra, P.C. Huijgens, and G.A. van Dongen. Preparation and evaluation of (89)zr-zevalin for monitoring of (90)y-zevalin biodistribution with positron emission tomography. *Eur J Nucl Med Mol Imaging*, 33:1337–1345, 2006.

[39] C.R. Divgi, N. Pandit-Taskar, A.A. Jungbluth, V.E. Reuter, M. Gnen, S. Ruan, C. Pierre, A. Nagel, D.A. Pryma, J. Humm, S.M. Larson, L.J. Old, and P. Russo. Preoperative characterisation of clear-cell renal carcinoma using iodine-124-labelled antibody chimeric g250 (124i-cg250) and pet in patients with renal masses: a phase i trial. *Lancet Oncol*, 8:304–310, 2007.

[40] T.H. Oude Munnink, E.C. Dijkers, S.J. Netters, M.N. Lub de Hooge, A.H. Brouwers, J.G. Haasjes, C.P. Schrder, and E.G. de Vries. Trastuzumab pharmacokinetics influenced by extent human epidermal growth factor receptor 2-positive tumor load. *J Clin Oncol*, 28:e355–e356, 2010.

[41] S.N. Rizvi, O.J. Visser, M.J. Vosjan, A. van Lingen, O.S. Hoekstra, J.M. Zijlstra, P.C. Huijgens, G.A. van Dongen, and M. Lubberink. Biodistribution, radiation dosimetry and scouting of 90y-ibritumomab tiuxetan therapy in patients with relapsed b-cell non-hodgkin's lymphoma using 89zr-ibritumomab tiuxetan and pet. *Eur J Nucl Med Mol Imaging*, 39:512–520, 2012.

[42] C.C. Watson, C. Hayden, M.E. Casey, J. Hamill, and B. Bendriem. Prompt gamma correction for improved quantification in 82rb pet. *J Nucl Med*, 49:64P, 2008.

[43] M. Lubberink, H. Schneider, M. Bergstrom, and H. Lundqvist. Quantitative imaging and correction for cascade gamma radiation of 76br with 2d and 3d pet. *Phys Med Biol*, 47:3519–3534, 2002.

[44] J. De Beenhouwer, S. Staelens, S. Vandenberghe, J. Verhaeghe, R. Van Holen, E. Rault, and I. Lemahieu. Physics process level discrimination of detections for gate: assessment of contamination in spect and spurious activity in pet. *Med Phys*, 36:1053–1060, 2009.

[45] S. Walrand, F. Jamar, I. Mathieu, J. De Camps, M. Lonneux, M. Sibomana, D. Labar, C. Michel, and S. Pauwels. Quantitation in pet using isotopes emitting prompt single gammas: application to yttrium-86. *Eur J Nucl Med Mol Imaging*, 30:354–361, 2003.

[46] B.J. Beattie, R.D. Finn, D.J. Rowland, and K.S. Pentlow. Quantitative imaging of bromine-76 and yttrium-86 with pet: a method for the removal of spurious activity

introduced by cascade gamma rays. *Med Phys*, 30:2410–2423, 2003.

[47] R.A. Gregory, C.A. Hooker, M. Partridge, and G.D. Flux. Optimization and assessment of quantitative 124i imaging on a philips gemini dual gs pet/ct system. *Eur J Nucl Med Mol Imaging*, 36:1037–1048, 2009.

[48] M.G. Stabin, R.B. Sparks, and E. Crowe. Olinda/exm: the second-generation personal computer software for internal dose assessment in nuclear medicine. *J Nucl Med*, 46:1023–1027, 2005.

[49] G. Sgouros. Bone marrow dosimetry for radioimmunotherapy: theoretical considerations. *J Nucl Med*, 34:689–694, 1993.

[50] C. Hindorf, O. Linden, J. Tennvall, K. Wingardh, and S.E. Strand. Time dependence of the activity concentration ratio of red marrow to blood and implications for red marrow dosimetry. *Cancer*, 94(4 Suppl):1235–1239, 2002.

[51] J. Schwartz, J.L. Humm, C.R. Divgi, S.M. Larson, and J.A. O'Donoghue. Bone marrow dosimetry using 124i-pet. *J Nucl Med*, 53:615–621, 2012.

[52] G. Sambuceti, M. Brignone, C. Marini, M. Massollo, F. Fiz, S. Morbelli, A. Buschiazzo, C. Campi, R. Piva, A.M. Massone, M. Piana, and F. Frassoni. Estimating the whole bone-marrow asset in humans by a computational approach to integrated pet/ct imaging. *Eur J Nucl Med Mol Imaging*, 39:1326–1338, 2012.